Modelling and control of an adaptive tuned mass damper based on shape memory alloys and eddy currents

M. Berardengo, A. Cigada, F. Guanziroli, S. Manzoni *

Politecnico di Milano, Department of Mechanical Engineering, Via La Masa, 34, 20156 Milan, Italy

Received 13 August 2014
Received in revised form 18 February 2015
Accepted 16 March 2015
Available online 3 April 2015

1. Introduction

The Tuned Mass Damper (TMD) to attenuate structural vibrations has been widely used in engineering since 1909, when Frahm [1] first designed the device coupling the use of a mass and a spring. A TMD can be designed with many different layouts and employing different physical principles, so that it can assume a variety of shapes. Notwithstanding, a TMD is usually modelled as a single degree-of-freedom (sdof) system, made up of a mass m, a damper with a damping constant c,

* Corresponding author. Tel.: +39 0223998589; fax: +39 0223998585.
E-mail address: stefano.manzoni@polimi.it (S. Manzoni).

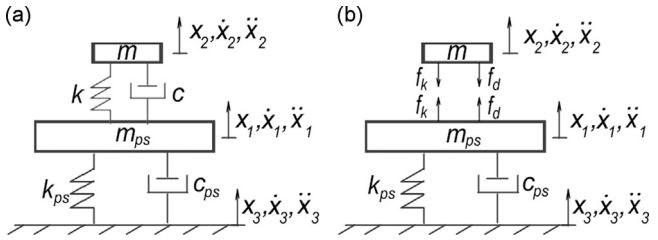

Fig. 1. Primary system with a TMD: lumped-parameters representation (a) and equivalent forces (b).

and a spring with an elastic constant k (Fig. 1); such is the one used in this present paper. It should be noted that in Fig. 1, m_{PS}, c_{PS}, and k_{PS} are respectively the mass, the damping coefficient and the elastic coefficient of the system to be controlled, while m, c, and k are respectively the mass, the damping coefficient and the elastic coefficient of the TMD. f_k and f_d are the elastic and damping force exchanged by the two systems respectively. Finally, x_1, x_2, and x_3 are respectively the displacement of m_{PS}, m and the constraint. Their first and second derivatives (represented respectively by a single dot and by two dots) are the corresponding velocities and accelerations.

In this situation, the basic principle of the TMD is that its eigenfrequency should be tuned to the resonance frequency of the system to be controlled, herein referred to as Primary System (PS). This tuning allows to attenuate the vibrations of the PS at such eigenfrequency. Modelling the PS as a sdof system, the whole structure composed by the PS and the TMD is as shown in Fig. 1a.

In Fig. 1a, the values of m, c, and k must be set so that the eigenfrequency of the TMD is tuned to the eigenfrequency of the PS, as abovementioned. If the disturbance is random (as in the case considered in this paper), a proper value for c should be calculated, so that the vibration of the PS is minimised within a frequency range around its resonance frequency.

Although TMDs can be very effective in reducing vibrations of the PS and optimisation of their features is widely studied (e.g. [2,3]), they do suffer from a major drawback: they cannot adapt their dynamic characteristics. Sometimes this disadvantage can constitute a critical problem, especially when the PS undergoes significant changes of its modal behaviour. For instance, major variations of the environmental temperature can cause significant changes in the eigenfrequency value of the PS, or even of the TMD itself, thus causing a mistuning between the resonance frequency of the PS and that of the TMD. Such a mistuning can render the TMD ineffective in reducing vibration.

Given the situation herein premised, great effort has gone into designing Adaptive TMDs (ATMDs), i.e. able to change their own modal characteristics in order to follow eventual changes of the modal behaviour of the PS. When a new ATMD is designed, the device is expected to be able to change either its eigenfrequency or its damping, and some devices are required and designed to change both parameters. The choice of which parameter must be adapted depends on the application and on the disturbance taken into account. The specific performance required of the ATMD leads to different approaches in its design, employing different solutions. Various different physical principles have been used to render a TMD adaptive, some of which are listed here:

- Longbottom et al. [4] and Long et al. [5] used pneumatic springs, whose stiffness can be tuned by changing the air pressure;
- Bonello et al. [6] and Gsell et al. [7] used piezo-ceramic actuators;
- Carneal et al. [8] and Brennan [9] used servo-actuators;
- Carpineto et al. [10] employed the hysteresis of short steel wire ropes;
- Weber et al. [11,12] used magnetorheological dampers;
- Heuss et al. [13] used piezoelectric transducers;
- Savi et al. [14], Aguiar et al. [15], Tiseo et al. [16], Mani and Senthilkumar [17], Zuo and Li [18], Rustighi et al. [19,20], Ozbulut et al. [21], Mavroidis [22], Senthilkumar and Umapathy [23], and Williams et al. [24,25], used shape memory alloys (SMA) to design and construct ATMDs capable of changing their eigenfrequency and, overall, to dampen vibrations in light structures, on account of the unique characteristics of such materials.

We have found this latter approach particularly promising, since SMAs are ever more widely used in engineering, they have physical properties which can be employed for vibration reduction, and they are cheaper than other materials. Furthermore, they are often produced in lightweight shapes (e.g. wires); this feature is crucial because it allows to construct adaptive devices avoiding load effects in light structures.

The aforementioned physical principles can be used to change either the eigenfrequency of the ATMD or its damping, and some can be even used for both these goals. Some more facts should be pointed out on the issue of damping adaptation. There are, in fact, other possible approaches to designing an adaptive damper and they have already been discussed in literature, including – yet not purposely considering – applications in ATMDs. Also these principles can be employed in rendering the TMD damping adaptive. For example, magnetic (e.g. [26]), liquid (e.g. [27,28]), or mechanical devices (e.g. [29]) can be employed. Also electro-magnetic principles, such as eddy currents, can be used. Eddy current dampers are effective in damping vibrations and are simple to model and drive compared to other kinds of aforementioned dampers (see

Section 3). Furthermore, they can be built with different shapes and sizes in order to fit them to different kinds of PSs. This makes them suitable for practical applications in vibration control.

This paper presents a new ATMD for light structures, which relies on the use of SMAs and eddy currents. The referenced works (e.g. [20]) employ SMAs to build beams, whose eigenfrequency can be changed by changing the material's Young's modulus (further details are provided in the following section). These beams, rigidly connected to the PS, constitute the TMD. Although these TMDs are effective, they do suffer some limitations: the range of adaptation of their eigenfrequency is limited, they require the use of high performance SMAs, and often the layout of the ATMD does not allow to add a device to change the damping as well. Thus, we see the scope for further improvements. Particularly, the goals of this paper are as follows:

1. achieving a range of adaptation of the ATMD eigenfrequency of at least 50% of its nominal value. This is achieved by using SMA wires, instead of SMA beams;
2. the TMD layout must not require high-performance SMAs (i.e. it must work properly with any kind of SMA material);
3. the ATMD must be able to adapt its eigenfrequency as well as its damping. Such a goal is achieved by designing an ATMD relying not only on SMAs, but also on an additional element (i.e. an eddy current damper).

These improvements would allow to properly attenuate the vibrations in a system subject to random excitation, which is the case considered in this paper. Indeed, the possibility to follow eventual changes of the PS and to adapt the damping of the ATMD are crucial features of any attempt to attenuate vibrations due to random disturbances.

The paper is organised as follows:

- Section 2 presents the main properties of SMAs, highlighting those considered and employed in the present work;
- Section 3 presents the physical principle chosen to adapt the damping of the ATMD;
- Section 4 shows the layout of the new ATMD and explains how a wide range of the ATMD resonance frequency is achieved. The main parameters influencing the working principle of the ATMD are here introduced as well. Furthermore, this section explains how the three abovementioned goals for the new ATMD are achieved;
- Section 5 provides details of the model developed to simulate the behaviour of the ATMD based on SMAs;
- Section 6 presents the algorithms employed to adapt the modal behaviour of the ATMD;
- Section 7 shows the experimental test set-up used to verify the effectiveness of the new ATMD;
- Section 8 presents a comparison between the results achieved by experimental tests and those obtained by numerical simulations.

2. Shape memory alloys

This section discusses the main features of SMAs [30], which are considered suitable for the purpose of the present paper and, more generally, to act on the dynamics of mechanical systems. The specific material used in this paper is Nitinol [30], constituted of nickel and titanium.

The main characteristic of SMAs is the possibility to change their composition between austenite and martensite phases by applying proper temperature and stress values. Fig. 2 clearly expounds the features of the SMAs. SMAs can assume three phases: detwinned martensite (DM), twinned martensite (TM), and austenite (AU). In Fig. 2, σ_s is the stress value at which

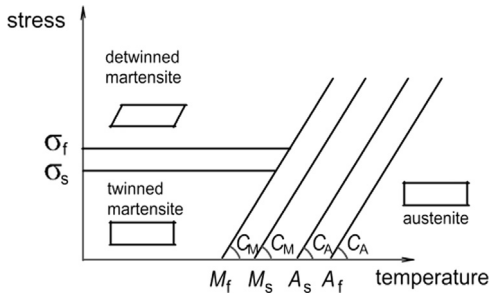

Fig. 2. SMA working principle.

Table 1
Technical data of the SMA material used, obtained by experimental tests.

A_s	A_f	M_s	M_f	C_A	C_M	H^{cur}	α	$E_{w,DM}$	$E_{w,AU}$
68.6 °C	78.9 °C	55.2 °C	42.7 °C	9.90 MPa/°C	6.83 MPa/°C	4.39%	10^{-6} °C^{-1}	32.1 GPa	39.5 GPa

the transformation from twinned to detwinned martensite starts at environmental temperature, while σ_f is the value at which the transformation is completed. A_s is the temperature value at which the transformation from twinned martensite to austenite starts at null stress, while A_f is the value at which the transformation is completed. M_s is the temperature value at which the transformation from austenite to twinned martensite starts at null stress, while M_f is the value at which the transformation is completed. C_A and C_M are the angular coefficients of the transformation lines.

Table 1 presents the values of the parameters shown in Fig. 2 for the SMA wires used in the present work, identified by means of experimental tests. In this table, H^{cur} is the current maximum transformation strain (i.e. the strain due to the change of shape between TM and DM), α is the thermal expansion coefficient, $E_{w,\text{DM}}$ and $E_{w,\text{AU}}$ are the Young's moduli of the DM and AU phases respectively.

Fig. 2 shows that the shape of the SMA can be changed by applying a stress value higher than σ_s (transformation from TM to DM) and that the original shape can be recovered by increasing the temperature (transformation from DM to AU). Then, by changing the temperature, it is possible to change phase between DM and AU and thus change shape. Fig. 2 illustrates that the shape in the TM and AU phases is the same (i.e. the unstrained shape).

The manner in which the properties of the SMA are employed in the new ATMD shall be explained in Section 4. At this point it is useful to point out that the abovementioned properties of the SMAs are used to change the eigenfrequency of the ATMD. The damping properties instead are changed employing an additional device, as explained in Section 3.

More extensive information about properties of SMAs can be found in [30].

3. Physical principle employed to adapt damping

There are several physical principles (as discussed in Section 1) which can be used to adapt the damping of the ATMD (i.e. to adapt c). Among these, the authors of these papers have focused on the principles which allow to generate a viscous damping force (i.e. a force proportional to velocity), do not require contact between two or more components, have a linear control law, and allow to use low-weight components. These characteristics are found in inductive and eddy current devices. The latter solution was adopted in this paper, also on account of the ease of design of such actuators. The reliability of damping devices based on eddy currents has already been proven by different works in literature (e.g. [31–33]).

The basic components of the damper are a coil, in which a DC current i_d flows, and a cylinder made of conducting material: the current flows through the coil generating a magnetic field so that, when the cylinder moves within it, a force f_d is generated acting in opposition to the relative velocity [33]. Fig. 3 explains the device layout and how the magnetic field is generated.

The damping force f_d assumes the following expression [33]:

$$f_d = -2\pi aB\left(\frac{2\pi aB}{\frac{2\pi a\rho}{h_{\text{ag}}d}}\right)\dot{x}_d \tag{1}$$

where a and d are respectively the inner radius and the thickness of the cylinder, h_{ag} is the height of the air-gap, ρ is the resistively of the cylinder material, B is the magnetic field in which the cylinder is immersed, and $\dot{x}_d$ is the relative velocity between the cylinder and the coil. Therefore, the damping coefficient is

$$c_d = \frac{2\pi a h_{\text{ag}} dB^2}{\rho} \tag{2}$$

The magnetic field B can be changed by changing the value of the current flowing in the coil. According to Eq. (2), this causes a change of the damping coefficient c_d. The relation between the current i_d and the magnetic field B can be calculated by solving the magnetic circuit and it has the following form [33]:

$$B = \frac{Ni_d}{A_{\text{ag}}\Theta} \tag{3}$$

where N is the number of turns of the coil, A_{ag} is the area of the air-gap, and Θ is the reluctance of the magnetic circuit.

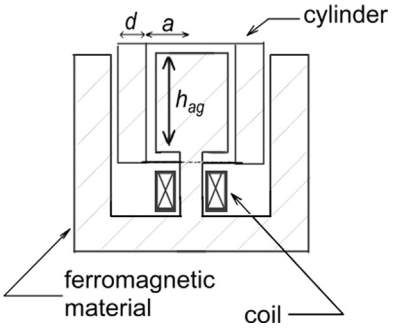

Fig. 3. Layout of the eddy current damper.

4. Layout of the new adaptive tuned mass damper

This section discusses the layout of the newly proposed ATMD, and the method employed to achieve extended frequency range is illustrated in particular.

The SMA-based ATMDs described in most of the referenced works are constituted by cantilever beams. The principle employed is the transformation between TM and AU, which can be achieved by changing the temperature of the SMA, without applying any stress (Fig. 2). Such a transformation determines a change of the Young's modulus of the SMA, which in turn determines a change of eigenfrequency of the beams and thus of the ATMDs.

This paper's proposition is to construct the ATMD with a central mass m linked to the PS by four SMA wires (Fig. 4). By means of elastic elements (Fig. 4), these wires are subject to pre-stress (and thus a pre-strain) above the value of σ_f (Fig. 2) in order to achieve the condition of DM. Then, the working principle of the ATMD relies on the transformation between DM and AU by means of a temperature change, which allows to change the shape (i.e. the length chiefly) of the wires and thus the axial tensile load F they are subject to. The change of the axial load F allows the change of the eigenfrequency of the ATMD [34]. Therefore, the working principle can be summarised as follows: a change of temperature causes a change of shape and consequently also a change of stress on the SMA wires. Particularly, when the wires are heated from DM to AU, they recover their initial shape (Fig. 2), thus their length decreases, and this causes a stretch of the spring and an increase of the axial load. Conversely, when the wires are cooled form AU to DM, their length increases and thus the springs shorten and the axial load decreases.

The new configuration here proposed allows to achieve a much wider frequency range of adaptation than would be possible by using cantilever beams. According to [34], the following relation is valid for the value of the first eigenfrequency ω_1 of a cantilever beam:

$$\omega_1 \sim \sqrt{E_b} \tag{4}$$

where E_b is the beam's Young's modulus. Relying for example on the beam used in [20,19], the Young's modulus was 59 GPa for AU and 40 GPa for TM. In these conditions, the possible variation of the ATMD eigenfrequency $R\omega$ is

$$R\omega = \frac{\omega_{1,\mathrm{AU}} - \omega_{1,\mathrm{TM}}}{\omega_{1,\mathrm{TM}}} \times 100 = \left(\frac{\sqrt{E_{b,\mathrm{AU}}}}{\sqrt{E_{b,\mathrm{TM}}}} - 1 \right) \times 100 = 21\% \tag{5}$$

where $\omega_{1,\mathrm{AU}}$ and $\omega_{1,\mathrm{TM}}$ are the value of the first eigenfrequency when the material is in AU and TM phases respectively. And $E_{b,\mathrm{AU}}$ and $E_{b,\mathrm{TM}}$ are the value of the Young's modulus of the beam when the material is in AU and TM phase respectively.

As for the new configuration proposed, the following relation is valid for ω_1, according to [34,35]

$$\omega_1 \sim \frac{\sqrt{F}}{(L_{\mathrm{wh}})^n} \tag{6}$$

where L_{wh} is the length of the SMA wire strained by the axial load F produced by the spring. n is a constant dependent on the boundary conditions of the wire; it is set to 0.5 throughout this whole section of the paper, because the other possible values (e.g. 1 [34]) achieve very similar results. Eq. (6) can be rearranged and expressed in terms of stress σ_w and strain ε_w on the wires:

$$\omega_1 \sim \frac{\sqrt{F}}{(L_{\mathrm{wh}})^{0.5}} = \frac{\sqrt{\sigma_w A_w}}{\sqrt{L_w(\varepsilon_w + 1)}} \tag{7}$$

where L_w is the length of the unstrained SMA wire and A_w is the double of the cross-section A_{w1} of the SMA wires (the change of cross-section due to strain is considered negligible to the purpose of the present paper). The reason for using A_w in

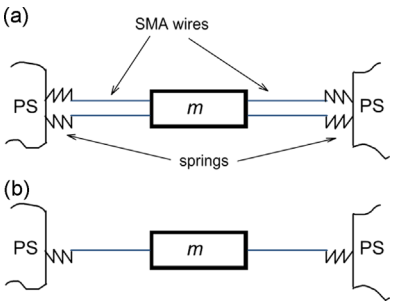

Fig. 4. Layout of ATMD based on SMA wires: top view (a) and lateral view (b).

place of A_{w1} is that the SMA wires are two for each side of the ATMD. Then, $R\omega$ can be achieved by means of Eq. (7):

$$R\omega = \frac{\omega_{1,\mathrm{AU}} - \omega_{1,\mathrm{DM}}}{\omega_{1,\mathrm{DM}}} \times 100 = \left(\frac{\sqrt{(\varepsilon_{w,\mathrm{DM}} + 1)\sigma_{w,\mathrm{AU}}}}{\sqrt{(\varepsilon_{w,\mathrm{AU}} + 1)\sigma_{w,\mathrm{DM}}}} - 1 \right) \times 100 \tag{8}$$

The values of stress and strain at which the SMA wires work in AU and DM phases must be known to solve Eq. (8) and find the value of $R\omega$. The values of $\sigma_{w,\mathrm{AU}}$ (i.e. the maximum stress value) and $\sigma_{w,\mathrm{DM}}$ (i.e. the minimum stress value) are set to 200 and 50 MPa respectively, since the operating stress range for the SMA wires suggested by the manufacturer is below 250 MPa. Furthermore, 50 MPa is over σ_f(Fig. 2). The strain can be expressed by the following general relation, according to [30]:

$$\varepsilon_w = \varepsilon_w^e + \varepsilon_w^t + \varepsilon_w^{th} = \frac{\sigma_w}{E_w} + H^{\mathrm{cur}}(\sigma) + \alpha(T - T_0) \tag{9}$$

where ε_w^e is the elastic strain component, ε_w^t is the strain component due to the thermo-elastic martensitic transformation [30] (i.e. the strain due to the change of shape from TM to DM. See Fig. 2), ε_w^{th} is the strain component due to the thermal expansion, E_w is the Young's modulus of the SMA wires (Table 1), $H^{\mathrm{cur}}(\sigma)$ is the current maximum transformation strain [30] (i.e. the strain due to the change of shape from TM to DM. See Table 1) [30], α is the thermal expansion coefficient of the SMA wires (Table 1), T is the temperature, and T_0 is the reference temperature (i.e. the environmental temperature of 20 °C). Relying on Eq. (9), we may obtain the expression of $\varepsilon_{w,\mathrm{DM}}$ and $\varepsilon_{w,\mathrm{AU}}$:

$$\varepsilon_{w,\mathrm{DM}} = \frac{\sigma_{w,\mathrm{DM}}}{E_{w,\mathrm{DM}}} + H^{\mathrm{cur}}(\sigma), \quad \varepsilon_{w,\mathrm{AU}} = \frac{\sigma_{w,\mathrm{AU}}}{E_{w,\mathrm{AU}}} + \alpha\left(T_{\mathrm{AU},200} - T_0\right) \tag{10}$$

In fact, the phase of the material is DM at environmental temperature (Fig. 2) and thus the thermal component can be neglected, while when the SMA wire is in AU phase it has recovered its original shape (Fig. 2) and thus ε_w^t is null. $T_{\mathrm{AU},200}$ is the temperature above which AU is the only existing phase at a stress of 200 MPa.

Relying on the data of the SMA wires used in this work (Table 1), identified by means of experimental tests, Eq. (10) can be substituted into Eq. (8) so that $R\omega$ can be calculated. The result is about 103%, which is much higher than the 21% of Eq. (5) and satisfies the goal set out in Section 1.

This demonstrates that the proposed layout and use of SMA wires allow to achieve a wide range of the eigenfrequency of the ATMD. Furthermore, the result of Eq. (8) mostly depends on the ratio between the two values of stress. This highlights another advantage of the proposed layout as compared to the other approaches referenced (Eq. (5)). Indeed, this stress ratio can be high enough to have a wide frequency range, regardless of the kind of SMA used. Conversely, the referenced approaches require high-performance SMAs to increase the adaptation frequency range, meaning that the difference between $E_{b,\mathrm{AU}}$ and $E_{b,\mathrm{TM}}$ must be as high as possible. In fact, it is easier to find SMA wires with a high stress ratio, rather than with a high difference between $E_{b,\mathrm{AU}}$ and $E_{b,\mathrm{TM}}$.

The key elements of the application herein presented are the elastic springs shown in Fig. 4, which allow to produce a change of F when the change of shape takes place during the transformation between DM and AU. Since the stress range for the material used in this work is 50–200 MPa, the springs are designed to have an elastic constant so that

- they generate a stress of 50 MPa in the wires, at environmental temperature, in order to have the SMA wires in DM phase;
- they guarantee a stress value of 200 MPa (i.e. the maximum stress value set in the case here considered) at 103.91 °C (i.e. $T_{\mathrm{AU},200}$). In fact, this is the temperature above which the SMA wires are in AU phase at 200 MPa. This temperature was estimated by means of experimental tests carried out on the wires employed.

The value of the constant K of each spring was calculated by imposing the equality between the displacement u of the outer end of the SMA wire, and the stretch q of the spring (exploiting the symmetry of the system; see Fig. 5):

$$u = -q \tag{11}$$

If the axial load F is changed from a situation of equilibrium (i.e. from F_1 to F_2, $F_2 - F_1 = \overline{\Delta}F$), then u and q are non-null quantities and a change of stress σ_w takes place (i.e. $\overline{\Delta}\sigma_w$). Consequently, there is change of the strain (i.e. $\overline{\Delta}\varepsilon_w$). Vice versa, if a $\overline{\Delta}\varepsilon_w$ occurs, a change of axial force F occurs as well. Thus, the following relations can be written according to Eq. (11):

$$\overline{\Delta}F = \overline{\Delta}\sigma_w A_{w1} = Kq = -Ku = -K\overline{\Delta}\varepsilon_w L_w \;\Rightarrow\; \overline{\Delta}\varepsilon_w = -\frac{\overline{\Delta}\sigma_w A_{w1}}{KL_w} \tag{12}$$

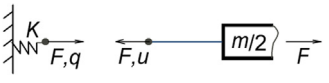

Fig. 5. Scheme for calculating K (view from the front side).

Therefore, if the phase of the wires is changed from DM to AU, the following expression is achieved (relying on Eqs. (10) and (12)):

$$-\frac{(\sigma_{w,\mathrm{AU}}-\sigma_{w,\mathrm{DM}})A_{w1}}{KL_w}=\left(\frac{\sigma_{w,\mathrm{AU}}}{E_{w,\mathrm{AU}}}+\alpha(T_{\mathrm{AU},200}-T_0)\right)-\left(\frac{\sigma_{w,\mathrm{DM}}}{E_{w,\mathrm{DM}}}+H^{\mathrm{cur}}(\sigma)\right) \tag{13}$$

Rearranging Eq. (13), the following expression is achieved:

$$K=\frac{(\sigma_{w,\mathrm{DM}}-\sigma_{w,\mathrm{AU}})A_{w1}}{\left(\frac{\sigma_{w,\mathrm{AU}}}{E_{w,\mathrm{AU}}}-\frac{\sigma_{w,\mathrm{DM}}}{E_{w,\mathrm{DM}}}+\alpha(T_{\mathrm{AU},200}-T_0)-H^{\mathrm{cur}}(\sigma)\right)L_w} \tag{14}$$

Eq. (14) allows to calculate the value of K by filling in all the required variables. The value obtained is 14628.5 N/m. The value used for L_w was 50 mm. The rational for this choice will be clarified in Section 7.

5. Model of the new adaptive tuned mass damper

According to Fig. 1b, two forces are exchanged between the TMD mass and the PS: an elastic force f_k, which depends on the relative displacement x between m and m_{PS} (i.e. $x=x_2-x_1$), and a damping force f_d, which depends on the relative velocity $\dot{x}$ between m and m_{PS}. The whole system is governed by the following dynamic equations:

$$\begin{cases} m_{\mathrm{PS}}\ddot{x}_1+c_{\mathrm{PS}}\dot{x}_1+k_{\mathrm{PS}}x_1-f_k(x,t)-f_d(\dot{x},t)=c_{\mathrm{PS}}\dot{x}_3+k_{\mathrm{PS}}x_3 \\ m\ddot{x}_2+f_k(x,t)+f_d(\dot{x},t)=0 \end{cases} \tag{15}$$

This system represents the case in which the vibration of the PS is due to ground excitation. If a force acts directly on the PS, it must simply replace the right-hand-side of the first equation.

The following sections discuss how these two forces, f_k and f_d, are generated and can be modelled. The damping force f_d is generated by the principle of eddy currents, while the elastic force f_k is generated by means of SMA wires.

5.1. Elastic force

Considering the ATMD mass in Fig. 6 (in which the system symmetry is employed and in which the first mode of the ATMD is considered) subject to the axial load F^* acting on the SMA wires, the angle of each wire, above the horizontal, can be expressed as

$$\lambda=\tan^{-1}\left(\frac{x}{L_{\mathrm{wh}}}\right) \tag{16}$$

where L_{wh} is the length of the wires when subject only to axial load F produced by the spring, without considering any other static or dynamic load. Thus, L_{wh} can be expressed as (employing Eq. (9))

$$L_{\mathrm{wh}}=(\varepsilon_w+1)L_w=\left(\frac{\sigma_w}{E_w}+\varepsilon_w^t+\alpha(T-T_0)+1\right)L_w \tag{17}$$

Therefore, f_k is

$$f_k(x,t)=4F^*(t)\sin\left(\tan^{-1}\left(\frac{x}{L_{\mathrm{wh}}}\right)\right) \tag{18}$$

The term 4 in Eq. (18) is due to the fact that two wires act on each side of m. F^* represents the variable value of F due to the static and dynamic loads (i.e. $F^*=F+\Delta F$, the symbol Δ expresses the changes due to the static and dynamic loads). Fixing the temperature of the wires and thus L_{wh}, the following relation is obtained:

$$L_{\mathrm{wd}}=\sqrt{x^2+L_{\mathrm{wh}}^2} \tag{19}$$

where L_{wd} is the length of the SMA wires subject to F^* and to vertical motion.

This variable can also be expressed as (employing Eq. (9))

$$L_{\mathrm{wd}}=(\Delta\varepsilon+1)L_{\mathrm{wh}}=\left(\Delta\varepsilon_w^e+\Delta\varepsilon_w^t+\Delta\varepsilon_w^{th}+1\right)L_{\mathrm{wh}}=\left(\frac{\Delta\sigma_w}{E_w}+\Delta\varepsilon_w^t+\Delta\varepsilon_w^{th}+1\right)L_{\mathrm{wh}}=\left(\frac{\Delta F}{E_wA_{w1}}+\Delta\varepsilon_w^t+\Delta\varepsilon_w^{th}+1\right)L_{\mathrm{wh}} \tag{20}$$

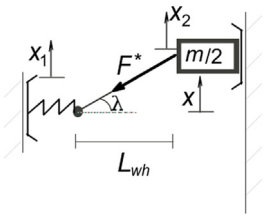

Fig. 6. Definition of the angle λ

where the symbol Δ again expresses the changes due to the static and dynamic loads.

Combining Eqs. (19) and (20) and assuming the temperature is fixed (i.e. $\Delta\varepsilon_w^{th}=0$) and that the value of ΔF is not high enough to produce change of material phase (i.e. $\Delta\varepsilon_w^{t}=0$), the following equation is obtained:

$$\left(\frac{\Delta F}{E_w A_{w1}}+1\right)L_{\mathrm{wh}}=\sqrt{x^2+L_{\mathrm{wh}}^2}\Rightarrow \Delta F=\frac{\sqrt{x^2+L_{\mathrm{wh}}^2}-L_{\mathrm{wh}}}{\frac{L_{\mathrm{wh}}}{E_w A_{w1}}} \tag{21}$$

Substituting Eq. (21) into Eq. (18), the following expression is obtained:

$$f_k(x,t)=4\left(F+\frac{\sqrt{x^2+L_{\mathrm{wh}}^2}-L_{\mathrm{wh}}}{\frac{L_{\mathrm{wh}}}{E_w A_{w1}}}\right)\sin\left(\tan^{-1}\left(\frac{x}{L_{\mathrm{wh}}}\right)\right) \tag{22}$$

Such an expression can be formulated as a Taylor series [36] around the position of equilibrium x_0:

$$f_k(x,t)\sim f_k(x_0)+\left.\frac{\mathrm{d}f_k}{\mathrm{d}x}\right|_{x_0}(x-x_0)+\left.\frac{1\,\mathrm{d}^2 f_k}{2\,\mathrm{d}x^2}\right|_{x_0}(x-x_0)^2+\cdots+\left.\frac{1\,\mathrm{d}^n f_k}{n!\,\mathrm{d}x^n}\right|_{x_0}(x-x_0)^n+\mathrm{O}(x^{n+1}) \tag{23}$$

The position x_0 can be obtained by solving the static equilibrium $mg=f_k(x_0)$ (where g is the gravity acceleration). This equation was evaluated both in the AU and DM phases, and in both cases x_0 is very close to zero (about 0.3 mm for DM and 0.12 mm for AU). Hence, x_0 was set to zero here (the solution of the static equilibrium requires to know all the parameters of the system. Some of them were already given in Table 1 and in the previous sections; others, such as m, will be given in Section 7). Therefore, x_0 is set to zero from here on, in this paper.

Finally, substituting Eq. (22) into Eq. (23) and ignoring terms higher than the third order, the dynamic part of f_k can be approximated as

$$f_k(x,t)=4\left[\frac{F}{L_{\mathrm{wh}}}x-\left(\frac{F}{2L_{\mathrm{wh}}^3}-\frac{E_w A_{w1}}{2L_{\mathrm{wh}}^3}\right)x^3\right] \tag{24}$$

In the present application Eq. (24) can be simplified considering only the linear term in x, because the cubic term proves to be negligible. Therefore

$$f_k(x,t)=4\frac{F}{L_{\mathrm{wh}}}x \tag{25}$$

Eq. (24) shows that the elastic force depends on F, L_{wh}, and E_w. These three variables depend on the phase of the SMA wires and such a phase can be AU, DM, or a combination of the two, depending on the temperature and stress on the wires. The next sections (5.1.1 and 5.1.2) describe how to change the three variables by means of the Joule effect. In fact, a current i_w runs through the wires and this generates heat by Joule effect. The consequent change of temperature T causes a change of phase and thus a change of F, L_{wh}, and E_w. Section 5.1.1 shows how to link T to F, L_{wh}, and E_w. Then, Section 5.1.2 discusses how to describe the relationship between i_w and T. Therefore a global model will be expounded, explaining how to relate the control variable i_w and the elastic force f_k.

5.1.1. *Material model: stress–temperature relation*

A key aspect to consider, in order to properly describe the behaviour of the SMA wires, is the relationship which links the temperature on a wire T and its stress σ_w. A change of T can cause a change of shape (i.e. length) and thus a change of the axial load produced by the spring (Fig. 4). Elucidating the relation between T and σ_w, also the relation between T and the variables F, L_{wh} and E_w can be calculated.

The starting point for such a model is the Experimentally-Based 1-D Material Model [30], which relies on the martensite volume fraction ξ (i.e. $\xi=0$ when the material is fully austenitic, and $\xi=1$ when it is fully martensitic) and is based on the following hypotheses:

1. The Young's modulus of the SMA material E_w is linearly dependent on ξ:

$$E_w=E_{w,\mathrm{AU}}-\xi\left(E_{w,\mathrm{AU}}-E_{w,\mathrm{DM}}\right) \tag{26}$$

2. The thermal expansion coefficient α is constant
3. The transformation strain linearly depends on ξ:

$$\varepsilon_w^t=\xi H^{\mathrm{cur}} \tag{27}$$

4. The starting and ending transformation temperatures (i.e. M_s^σ, M_f^σ, A_s^σ, A_f^σ) linearly depend on σ_w:

$$M_s^\sigma=M_s+\frac{\sigma_w}{C_M},\quad M_f^\sigma=M_f+\frac{\sigma_w}{C_M},\quad A_s^\sigma=A_s+\frac{\sigma_w}{C_A},\quad A_f^\sigma=A_f+\frac{\sigma_w}{C_A} \tag{28}$$

5. The value of ξ during the transformations from martensite to austenite (i.e. $\dot{T} > 0$) is described as [30]

$$\xi = \begin{cases} 1, & T \le A_s^\sigma \\ \frac{A_f^\sigma - T}{A_f - A_s}, & A_s^\sigma < T < A_f^\sigma \\ 0, & T \ge A_f^\sigma \end{cases} \tag{29}$$

And for the transformation from austenite to martensite (i.e. $\dot{T} < 0$) by

$$\xi = \begin{cases} 0, & T \ge M_s^\sigma \\ \frac{M_s^\sigma - T}{M_s - M_f}, & M_f^\sigma < T < M_s^\sigma \\ 1, & T \le M_f^\sigma \end{cases} \tag{30}$$

Eqs. (29) and (30) are valid only for transformations starting from a homogenous material and they do not take into account partial transformation. This model (particularly Eqs. (29) and (30)) has been refined in the herein study so to take into account also transformations starting from non-homogeneous material (partial transformations).

This new formulation assumes that a transformation can start from a non-homogeneous material. The starting martensite volume fraction is indicated as ξ_{-1} and the new formulation for transformations from martensite to austenite (i.e. $\dot{T} > 0$) is

$$\xi = \begin{cases} \xi_{-1}, & T \le A_s^\sigma \\ \frac{A_f^\sigma - T}{A_f - A_s}\xi_{-1}, & A_s^\sigma < T < A_f^\sigma \\ 0, & T \ge A_f^\sigma \end{cases} \tag{31}$$

And for transformations from austenite to martensite (i.e. $\dot{T} < 0$), it is

$$\xi = \begin{cases} \xi_{-1}, & T \ge M_s^\sigma \\ \frac{M_s^\sigma - T}{M_s - M_f}(1-\xi_{-1}) + \xi_{-1}, & M_f^\sigma < T < M_s^\sigma \\ 1, & T \le M_f^\sigma \end{cases} \tag{32}$$

Now Eqs. (31) and (32) can be used to find the relation between T and σ_w. Relying on Eq. (9) and Eq. (12), a generic equation describing the behaviour of the material due to a change of temperature is described as

$$-\frac{(\sigma_w - \sigma_{w,0})A_{w1}}{KL_w} = \frac{\sigma_w}{E_w} - \frac{\sigma_{w,0}}{E_{w,\mathrm{DM}}} + \alpha(T - T_0) + \varepsilon_w^t - \varepsilon_{w,0}^t \tag{33}$$

where $\sigma_{w,0}$ indicates the stress at environmental temperature (i.e. 50 MPa, see Section 4) and $\varepsilon_{w,0}^t = H^{\mathrm{cur}}$. On the grounds of Eqs. (26) and (27), Eq. (33) can be written as

$$\sigma_w(T) = \frac{\sigma_{w,0}\left(\frac{A_{w1}}{KL_w} + \frac{1}{E_{w,\mathrm{DM}}}\right) - \alpha(T - T_0) + H^{\mathrm{cur}}(1-\xi)}{\frac{A_{w1}}{KL_w} + \frac{1}{E_{w,\mathrm{AU}} - \xi(E_{w,\mathrm{AU}} - E_{w,\mathrm{DM}})}} = y + bT \tag{34}$$

The constants b and y are defined in Appendix A. When the material is out of the transformation region, ξ is at a constant value ξ_{-1} and the stress depends linearly on the temperature T, because of the effect of thermal expansion. On the contrary, when the material is under transformation, ξ is described by the second condition of Eq. (31) for transformations from DM to AU, or of Eq. (32) for transformations from AU to DM. Therefore, the expression of $\sigma_w(T)$ is achieved by substituting the second condition of Eq. (31), or the second condition of Eq. (32), into Eq. (34). The following relation is achieved for transformation from AU to DM:

$$\sigma_w(T) = \frac{-(b_{1,d} + b_{2,d}T) + \sqrt{(b_{1,d} + b_{2,d}T)^2 - 4a_d(c_{1,d} + c_{2,d}T + c_{3,d}T^2)}}{2a_d} \tag{35}$$

And the following for transformation from DM to AU:

$$\sigma_w(T) = \frac{-(b_{1,i} + b_{2,i}T) + \sqrt{(b_{1,i} + b_{2,i}T)^2 - 4a_i(c_{1,i} + c_{2,i}T + c_{3,i}T^2)}}{2a_i} \tag{36}$$

The terms in Eqs. (35) and (36) are given in Appendix B.

Therefore, Eqs. (34)–(36) describe the relationship between σ_w and T. Once the value of $\sigma_w(T)$ has been calculated, the value of F and L_{wh} can be computed as (see Eq. (17))

$$F = A_{w1}\sigma_w(T), \quad L_{\mathrm{wh}} = \left[\left(\frac{\sigma_w(T)}{E_w} + \alpha(T - T_0) + H^{\mathrm{cur}}\xi\right) + 1\right]L_w \tag{37}$$

The relationship between E_w and T can be found by means of Eqs. (31), (32), and (26).

Finally the elastic force f_k can be computed by means of either Eq. (24) or Eq. (25).

The final task herein set out to meet is how to control T. This is achieved by heating, by means of Joule effect, and by cooling by means of convection. The thermal model linking the current i_w supplied to the wires and T is described in the following Section 5.1.2.

5.1.2. Thermal model

The temperature T of the SMA wires can be changed employing two different principles: the Joule effect for heating, and convection for cooling. The first law of thermodynamics [37] can be applied to each wire:

$$\rho c_p \frac{\mathrm{d}T}{\mathrm{d}t} = \sigma_w \frac{\mathrm{d}\varepsilon_w}{\mathrm{d}t} - \frac{h s_{w,\mathrm{ext}}}{V_w}(T - T_0) + \frac{R_w i_w^2(t)}{V_w} \tag{38}$$

where ρc_p is the thermal capacity per unit of volume of the SMA wire, h is the convection coefficient of air, $s_{w,\mathrm{ext}}$ is the outer surface of each wire, R_w is the electric resistance of each wire, and V_w is the volume of each wire.

According to Eq. (12), the first term of the right-hand side of Eq. (38) can be rearranged as

$$\sigma_w \frac{\mathrm{d}\varepsilon_w}{\mathrm{d}t} = \sigma_w \frac{\mathrm{d}\varepsilon_w}{\mathrm{d}\sigma_w}\frac{\mathrm{d}\sigma_w}{\mathrm{d}T}\frac{\mathrm{d}T}{\mathrm{d}t} = \sigma_w \frac{-A_{w1}}{KL_w}\frac{\mathrm{d}\sigma_w}{\mathrm{d}T}\frac{\mathrm{d}T}{\mathrm{d}t} \tag{39}$$

As for Eq. (39), the term $\frac{\mathrm{d}\sigma_w}{\mathrm{d}T}$ can be calculated differentiating Eq. (34) for extra-transformation temperature changes, Eq. (35) for temperature changes during transformations from AU to DM, and Eq. (36) for temperature changes during transformations from DM to AU. The following formulations are achieved:

- Extra-transformation:

$$\frac{\mathrm{d}\sigma_w}{\mathrm{d}T} = b \tag{40}$$

- Transformation from AU to DM:

$$\frac{\mathrm{d}\sigma_w}{\mathrm{d}T} = \frac{2b_{2,d}\sqrt{A_{s,d}+T(B_{s,d}+C_{s,d}T)}+B_{s,d}+2C_{s,d}T}{4a_d\sqrt{A_{s,d}+T(B_{s,d}+C_{s,d}T)}} \tag{41}$$

- Transformation from DM to AU:

$$\frac{\mathrm{d}\sigma_w}{\mathrm{d}T} = \frac{2b_{2,i}\sqrt{A_{s,i}+T(B_{s,i}+C_{s,i}T)}+B_{s,i}+2C_{s,i}T}{4a_i\sqrt{A_{s,i}+T(B_{s,i}+C_{s,i}T)}} \tag{42}$$

The terms in Eqs. (41) and (42) are explained in Appendix C.

Then, Eq. (39) can be rearranged by using Eqs. (40) and (34) for extra-transformation temperature changes, Eqs. (41) and (35) for temperature changes during transformations from AU to DM and Eqs. (42) and (36) for temperature changes during transformations from DM to AU. Finally, Eq. (38) can be rewritten as

- Extra-transformation:

$$\rho c_p \frac{\mathrm{d}T}{\mathrm{d}t} = -\frac{A_{w1}}{KL_w}(y+bT)b\frac{\mathrm{d}T}{\mathrm{d}t} - \frac{h s_{w,\mathrm{ext}}}{V_w}(T-T_0) + \frac{R_w i_w^2(t)}{V_w} \tag{43}$$

Where the term ξ in the constants b and y is fixed to ξ_{-1}.

- Transformation from AU to DM:

$$\rho c_p \frac{dT}{\mathrm{d}t} = -\frac{A_{w1}}{KL_w}\frac{-(b_{1,d}+b_{2,d}T)+\sqrt{A_{s,d}+B_{s,d}T+C_{s,d}T^2}}{2a_d}\frac{2b_{2,d}\sqrt{A_{s,d}+T(B_{s,d}+C_{s,d}T)}+B_{s,d}+2C_{s,d}T}{4a_d\sqrt{A_{s,d}+T(B_{s,d}+C_{s,d}T)}}\frac{\mathrm{d}T}{\mathrm{d}t} - \frac{h s_{w,\mathrm{ext}}}{V_w}(T-T_0) + \frac{R_w i_w^2(t)}{V_w} \tag{44}$$

- Transformation from DM to AU:

$$\rho c_p \frac{\mathrm{d}T}{\mathrm{d}t} = -\frac{A_{w1}}{KL_w}\frac{-(b_{1,i}+b_{2,i}T)+\sqrt{A_{s,i}+B_{s,i}T+C_{s,i}T^2}}{2a_i}\frac{2b_{2,i}\sqrt{A_{s,i}+T(B_{s,i}+C_{s,i}T)}+B_{s,i}+2C_{s,i}T}{4a_i\sqrt{A_{s,i}+T(B_{s,i}+C_{s,i}T)}}\frac{\mathrm{d}T}{\mathrm{d}t} - \frac{h s_{w,\mathrm{ext}}}{V_w}(T-T_0) + \frac{R_w i_w^2(t)}{V_w} \tag{45}$$

Eqs. (43)–(45) describe the link between the control variable i_w and the temperature T of the SMA wires.

5.2. Damping force

Section 5.1 and its subsections have described how to link the control variable (i.e. i_w) to the elastic force acting on the PS. This present section faces the same issue relatively to the damping force f_d. The physical principle used to generate and change damping in the ATMD is that of eddy currents (see Section 3).

Eqs. (2) and (3) have illustrated how to generate a damping force $u_d = c_d\dot{x}$. In the present application a slight modification has been introduced: in fact, a permanent magnet (generating a magnetic field B_{mp}) has been introduced in addition to the coil producing the main variable magnetic field. This provides two benefits. Firstly, it allows to always have a base level of damping, which can then be increased making current flow through the coil. Moreover, the number of turns of the coil N and the current i_d necessary to obtain a given value of damping force f_d can both be reduced, consequently resulting in a simplification of the damper construction and fewer problems associated with heating.

The electrical equivalent of the coil can be represented as the series of an inductance and a resistance. Such a circuit is supplied by a voltage source and thus the dynamic equation governing the circuit is

$$L_c\frac{di_d(t)}{dt}+R_c i_d(t) = V(t) \tag{46}$$

where L_c is the inductance due to the coil, R_c is the resistance due to its turns, and V is the supplied voltage.

Employing Eqs. (2) and (3), the force f_d can be expressed as

$$f_d = \frac{-2\pi a h_{\mathrm{ag}} d\left[\left(\frac{Ni_d}{A_{\mathrm{ag}}\Theta}+B_{\mathrm{mp}}\right)^2\right]}{\rho}\dot{x} \Rightarrow c_d = \frac{2\pi a h_{\mathrm{ag}} d\left[\left(\frac{Ni_d}{A_{\mathrm{ag}}\Theta}+B_{\mathrm{mp}}\right)^2\right]}{\rho} \tag{47}$$

Eqs. (46) and (47) link the control variable V and the damping force f_d. Indeed, Eq. (46) allows to calculate i_d for a certain supplied $V(t)$ and then Eq. (47) allows to compute the force f_d produced by i_d.

6. Control algorithms

This section describes the control strategies devised to adapt the ATMD natural frequency and damping to the characteristics of the PS. Two different kinds of algorithms (APP1 and APP2 herein) were developed and tested to adapt the behaviour of the ATMD: they are described in Sections 6.1 and 6.2. In both the approaches, first the eigenfrequency of the ATMD is tuned and then the damping is adjusted. The first of the two strategies is based on an on-line identification of the PS features and on the consequent adaptation of the ATMD. The second strategy does not require any identification and is based on the shape of the power-spectrum of the vibration of the PS.

6.1. First control algorithm

The first approach (APP1) requires to estimate the dynamic parameters of the PS and to tune those of the ATMD in order to satisfy the optimisation criterion suggested in [38]. This approach requires an on-line estimation of different variables of the systems (Section 6.1.1) and the measurement of x_1, x_2, and x_3 (Fig. 1).

The optimal values of the dynamic features of the ATMD as a function of the PS characteristics are given in Ref. [38]:

$$\omega_{\mathrm{ATMD}} = \frac{\omega_{\mathrm{PS}}}{1+\frac{m}{m_{\mathrm{PS}}}}, \quad \xi_{\mathrm{ATMD}} = \sqrt{\frac{3\frac{m}{m_{\mathrm{PS}}}}{8\left(1+\frac{m}{m_{\mathrm{PS}}}\right)}} \Rightarrow c_{\mathrm{ATMD}} = 2m\omega_{\mathrm{ATMD}}\sqrt{\frac{3\frac{m}{m_{\mathrm{PS}}}}{8\left(1+\frac{m}{m_{\mathrm{PS}}}\right)}} \tag{48}$$

where ω_{PS} is the eigenfrequency of the PS, while ω_{ATMD} and ξ_{ATMD} are the eigenfrequency and the non-dimensional damping ratio of the ATMD, respectively. The conditions of Eq. (48) are for an undamped PS and thus valid in the practical applications where the damping of the PS (i.e. ξ_{PS}) is low. In the test-case herein used (see Section 7), the damping was low enough. If this were not the condition, different formulas for the optimal values can be used (e.g. [2]).

Employing Eq. (25) and the first condition of Eq. (48), the optimal value of F is

$$F_{\mathrm{opt}} = \frac{\omega_{\mathrm{PS}}^2 m_{\mathrm{PS}}^2 L_{\mathrm{wh}} m}{4(m+m_{\mathrm{PS}})^2} \tag{49}$$

Therefore, the controller must tune F in order to make it as close as possible to F_{opt} and F can be changed by adjusting i_w (see Section 5.1). The second condition of Eq. (48) provides the optimal value for the damping of the ATMD (Eqs. (46) and (47)); such a value can be reached by controlling the current i_d and thus the voltage V.

The procedure described above evidences that an on-line estimation of m_{PS} and ω_{PS} (Eq. (48)) is required (i.e. they are assumed to be unknown a priori). Then, two different choices are viable: using a model-based control to adapt F and c, or else a non-model-based control. The latter option has herein been opted for (i.e. non-model-based control), although the models in Section 5 have been validated as well (see Section 8). The use of a model-based controller would have required to employ Eqs. (34)–(36) to link σ_w and T, and Eqs. (43)–(45) to link T and the control variable i_w, which would have made for a much more complicated implementation of the controller itself. On the contrary, the non-model-based approach allows to

employ a simpler controller in practical applications, though a model-based controller could eventually be employed and would still prove reliable.

The values of m and of L_{wh} are known. In fact, although L_{wh} changes with temperature T (Eq. (37)), these changes are so small that they can be neglected in Eq. (49). The value of L_{wh} is thus fixed to a nominal value (see Section 7) when computing F_{opt}.

The following section describes how to estimate on-line m_{PS}, ω_{PS}, and the actual values of F and c. Then Sections 6.1.2 and 6.1.3 explain the kind of control used to drive the SMA wires and the eddy current damper, in order to reach the optimal values of Eqs. (48) and (49).

6.1.1. On-line estimation of parameters

Employing Eq. (15), the two of them can be summed, giving a further equation in which the terms dependent on f_k and f_d are removed. The second equation of the system can be rearranged employing Eq. (25). Finally, the following system of equations (expressed in matrix form) is obtained:

$$\begin{cases} \ddot{x}_1 = \begin{bmatrix} (-m\ddot{x}_2 - c_{PS}\dot{x}_1 + c_{PS}\dot{x}_3) & (x_3 - x_1) \end{bmatrix} \begin{bmatrix} m_{PS}^{-1} \\ \omega_{PS}^2 \end{bmatrix} \\ \ddot{x}_2 = \begin{bmatrix} \left(\frac{\dot{x}_1 - \dot{x}_2}{m}\right) & \left(\frac{4(x_1 - x_2)}{L_{wh} m}\right) \end{bmatrix} \begin{bmatrix} c \\ F \end{bmatrix} \end{cases} \tag{50}$$

The first equation of this system can be used to estimate m_{PS} and ω_{PS}, while the second is employed to estimate c and F. In this paper the accelerations are measured, and velocities and displacements are computed by integrating acceleration signals. All the terms in the raw vectors are assumed to be known, while those in the column vectors as unknown.

The algorithm used for on-line estimation is the gradient estimator [39]. Such a method requires to compare a measured signal (i.e. $\ddot{x}_1$ for the first equation of system 50 and $\ddot{x}_2$ for the second one) with an estimate of this signal dependent on the unknown parameters (i.e. this estimate is achieved by means of the equations in system 50 in this case). The convergence of the algorithm allows to obtain an on-line estimate of the values of m_{PS}, ω_{PS}, c, and F.

It is worth remarking that the measured signals are band-pass filtered around the resonance frequency of interest (cut-off frequencies equal to 10 and 30 Hz in this case, see Section 7) before being processed in order to remove the influence of the other modes of the PS. Obviously, this requires to have a rough knowledge of the eigenfrequency value associated to the mode to control.

6.1.2. Control of the SMA wires

As soon as the value of F and F_{opt} are achieved by means of the on-line estimation procedure and Eq. (49), the control of the SMA wires is activated in order to make F reach F_{opt}. Then, this control continuously works thanks to a continuous estimation of the actual value of F, m_{PS}, ω_{PS}, and F_{opt}.

The control strategy chosen to drive the current i_w is a gain-scheduling control [39], in which two regions were identified relying on an error signal. This error $e(t)$ is defined as

$$e(t) = F_{opt}(t) - F(t) \tag{51}$$

The two regions are defined as

- Region 1: $e(t) > \text{tol}$
- Region 2: $e(t) < -\text{tol}$

where tol is a fixed tolerance value. The interval $\pm$ tol is centred around zero.

In both the regions a proportional integral control was used:

$$i_w(t) = i_{w0} + k_{pcw} e(t) + k_{icw} \int e(t) dt \tag{52}$$

where i_{w0} is a constant current (its value depends on the region the controller is working in), k_{pcw} is the proportional coefficient of the controller, and k_{icw} is its integral coefficient. Both the values of k_{pcw} and k_{icw} depend on the region the controller is working in.

Before continuing, it is worth explaining why a gain-scheduling approach was chosen. In theory, a proportional integral control without gain-scheduling could be employed for controlling the SMA wires. Nevertheless, gain-scheduling is a proper tool for making the adaptation of the ATMD faster and more effective. The first advantage provided by such an approach is that k_{pcw} and k_{icw} can be fixed to different values in the two mentioned regions; this aspect is important since the two physical phenomena used to change the temperature of wires are different: the Joule effect to heat and convection to cool. This difference requires different values of k_{pcw} and k_{icw} to be used in the two regions, to optimise the performances of the controller. Furthermore, when a mistuning between the PS and the ATMD takes place (i.e. $|e(t)| > 0$) and the sign of the signal $e(t)$ changes, the phase of the SMA wires must be changed to reach tuning again. Therefore, the idea is to quickly

change the value of i_w in order to ensure fast adaptation. Since there are two phases of the SMA wires, two regions are defined (see above) and the following criteria are used:

- When the axial load is too high (i.e. $e(t) < -\text{tol}$, see Eq. (51)), the temperature T and the current i_w must be lowered. Thus, the value of i_{w0} in this region should be low, allowing to shift quickly towards DM (this causes the wires to increase their length: thus the springs shorten and the axial load decreases).
- When the axial load is too low (i.e. $e(t) > \text{tol}$, see Eq. (51)), the temperature T and the current i_w must be increased. Thus, the value of i_{w0} in this region should be high, allowing to shift quickly towards AU (this causes the wires to decrease their length: thus the springs stretch and the axial load increases).

This allows to avoid the use of a derivative term in the controller. In fact, a derivative term would have allowed a faster adaptation but could cause errors in the steady state condition [40]. The use of the gain-scheduling approach, as here discussed, allows to avoid using the derivative term, even ensuring fast adaptation.

In the considered test-case (see Section 7), the values of i_{w0} in the two regions have been chosen so to drive the system quickly towards the transformation regions, as already mentioned: i_{w0} must have values by which the temperature T is 80 °C for region 1 (i.e. towards AU) and 75 °C for region 2 (i.e. towards DM) (Fig. 7). The electric current values corresponding to these temperatures were calculated by means of Eq. (38) in steady state condition (i.e. with the derivative terms equal to zero) and resulted to be 1.05 and 0.95 A respectively. The temperature values (i.e. 75 and 80 °C) were specifically selected for the considered test-case (see Section 7): for different applications different values can be used.

When $e(t)$ is close to zero within the fixed tolerance, the controller maintains the last value of supplied current.

6.1.3. Control of the eddy current damper

The eddy current damper is controlled by means of a proportional integral control on the control variable V as well:

$$V(t) = k_{\text{pcd}} e_d(t) + k_{\text{icd}} \int e_d(t)dt \tag{53}$$

where k_{pcd} is the proportional coefficient of the controller and k_{icd} is its integral coefficient; e_d is an error signal defined as

$$e_d(t) = 2m\omega_{\text{ATMD}}(t)\xi_{\text{ATMD}}(t) - c(t) = c_{\text{ATMD}}(t) - c(t) \tag{54}$$

6.2. Second control algorithm

The second approach (APP2) relies on the shape of the power-spectrum of x_1 (see Fig. 1): the heights of the peaks $P1$ and $P2$ (Fig. 8) must be equal (i.e. optimisation of the eigenfrequency of the ATMD in order to achieve the best vibration reduction at resonance) and the height of point $P3$ (Fig. 8) must be close to those of $P1$ and $P2$, within a certain set tolerance value (i.e. optimisation of the damping of the ATMD). First the condition on $P1$ and $P2$ is resolved and then the height of $P3$ is tuned. APP2 requires to measure only x_1 and does not require to carry out an on-line estimation. Since APP2 works on the shape of the power-spectrum, it is most effective when the random disturbance (as in the case here considered, see Section 1) on the PS is close to white noise over the considered frequency range. This is a reasonable assumption because the considered frequency range is limited (i.e. few Hertz) in TMD applications. If this should not be the case, the same control strategy must be applied to the FRF x_1/x_3 and the measurement of x_3 will be necessary.

Control of the SMA wires has been carried out once again with a gain-scheduling control (Section 6.1.2) in which – in this case – the error signal $e(t)$ is defined as

$$e(t) = h_{P2}(t) - h_{P1}(t) \tag{55}$$

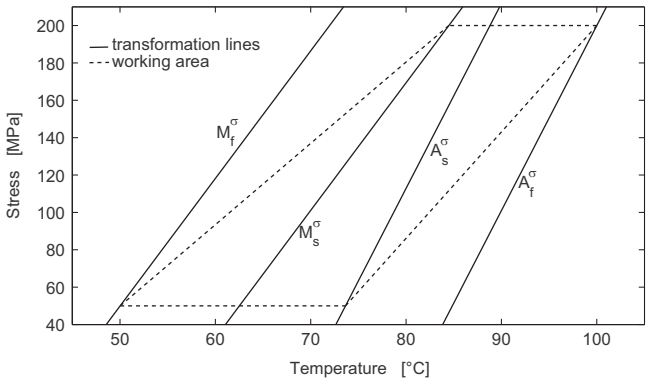

Fig. 7. Working area of the SMA wires.

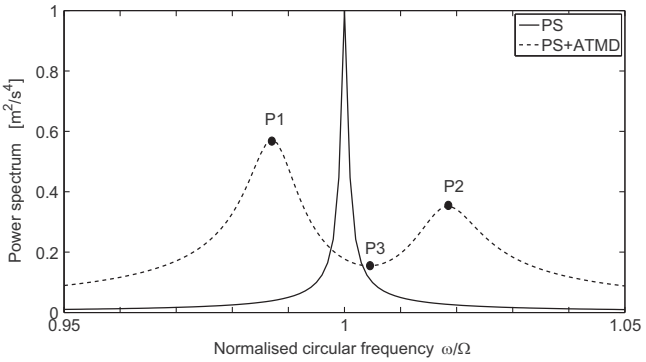

Fig. 8. Power spectrum of x_1 (see Fig. 1) of a generic structure. Points $P1$ and $P2$ are the maxima, while $P3$ is the minimum between the maxima.

where h_{P1} and h_{P2} are the heights of $P1$ and $P2$ respectively. The control of the damper is once again proportional integral (Section 6.1.3), in which – this time – the error $e_d(t)$ is defined as

$$e_d(t) = \frac{h_{P2}(t) + h_{P1}(t)}{2} - h_{P3}(t) \tag{56}$$

where h_{P3} is the height of $P3$.

The power-spectrum is a variable defined by an average procedure [41]. In this case the power-spectra are computed with time-windows of 50 s and by 10 averages. These values are closely subordinate to the particular system under investigation (see Section 7), since the number of averages needed to achieve a reliable estimation of the power-spectrum strongly depends on the signal-to-noise-ratio and the time length on the required frequency resolution.

7. Test case structure

A scheme of the system used for testing the new ATMD is shown in Fig. 9a. It has been designed with the simplest layout possible. Fig. 9b shows the PS with the ATMD mounted on it. In case of a generic PS a frame to mount the ATMD should be designed as well.

The eddy current damper is constructed by binding the cylinder to the mass of the ATMD and the coil to the PS.

The excitation applied was random and provided by means of an electro-dynamic shaker placed close to the PS and on the same substructure. The disturbance produced by the motion of the shaker propagated along the substructure made the PS vibrate. Therefore, the disturbance was a base excitation.

Table 2 summarises the nominal data used to design and construct the PS and the ATMD. These data refer to variables mentioned in the previous sections. The mode to be controlled is vertical with a resonance frequency at about 19 Hz and an associated non-dimensional damping ratio of about 0.48%.

The values of m and L_w were selected in order to place the first eigenmode of the ATMD (Fig. 4) around the resonance to be controlled and to have a ratio between m_{PS} and m close to 20, as indicated in the literature.

The four SMA wires are electrically connected in series, so to have the same current i_w flowing through them. The electric resistance R_w of each SMA wire is about 0.4 Ω.

As for the eddy current damper, the design here proposed allows to reach a damping coefficient c_d of about 4.6 N/m/s with a supply current i_d of 1 A (Eq. (47)). It should be remarked that this kind of actuator allows to greatly modify such a value merely by changing its geometry and the number of turns of the coil.

8. Experimental tests

This section presents the results of experimental tests aimed at validating the models developed to describe the behaviour of the SMA wires (Sections 5.1, 5.1.1 and 5.1.2) and at testing the effectiveness of the control methods proposed in Section 6.

First, experimental tests were carried out without the damper (Section 8.1), then also the damper was used and the whole ATMD was tested (Section 8.2).

In all the cases accelerometers were used to measure $\ddot{x}_1$, $\ddot{x}_2$, and $\ddot{x}_3$. The technical data of these transducers are provided in Table 3. Moreover, the axial load on the SMA wires was monitored by means of strain gauges forming calibrated half Wheatstone bridges [42] on the elastic elements of the ATMD (Fig. 9). Finally, also the input currents to the SMA wires and the eddy current damper were measured throughout the tests. All the signals were acquired by means of a 24 bit analog-to-digital acquisition board (with anti-aliasing filters on board). The sampling frequency was 2048 Hz. The real-time control of the SMA wires and the eddy current damper (as well as the acquisition of the signals) was managed by a Field Programmable Gate Array (FPGA) device.

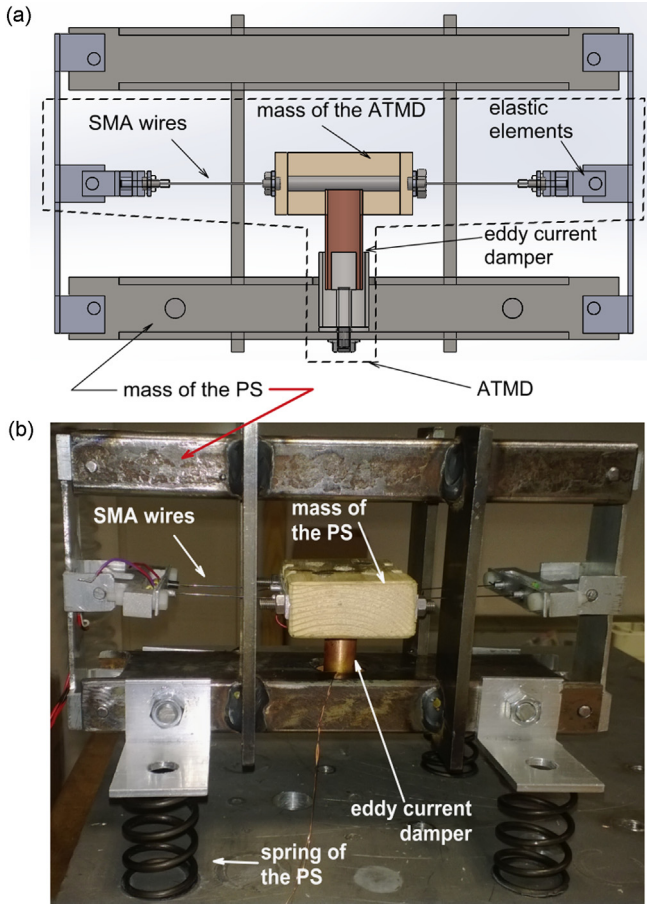

Fig. 9. PS coupled to the ATMD: (a) representation of the system (the mass of the PS is laid down on four springs), and (b) photo of the actual system (the picture was taken with a stress in the SMA wires lower than 50 MPa).

Table 2
Nominal data of the experimental set-up.

m_{PS}	m	L_w	Diameter of the SMA wires	K	N	a	h_{ag}	D	B_{mp}
1.95 kg	100 g	50 mm	0.5 mm	14628.5 N/m	500	6 mm	15 mm	1.5 mm	0.179 T

8.1. *Tests without the damper*

The aim of these experiments was to validate the model describing the behaviour of the SMA wires (Section 8.1.1) and to test the effectiveness of the control algorithms used to adapt the eigenfrequency of the ATMD (Section 8.1.2).

8.1.1. *Validation of the model*

In this test the SMA wires were supplied with two different values of the current i_w:

- 0 A, corresponding to a temperature T equal to the environmental one. In this case the phase of the SMA wires is DM (Section 4);
- 1.55 A, corresponding to a temperature T of about 110 °C (at and above this temperature the transformation into AU is completed with a stress of about 200 MPa; see Section 4). Hence, in this case the phase of the SMA wires is AU.

Fig. 10 shows the experimental FRFs between x_3 and x_1 in the two cases and compares them with those achieved using the numerical model above discussed.

The match is good, proving the numerical model reliable and that it correctly describes the dynamic behaviour of the whole system (i.e. PS+SMA wires). Furthermore, the value of $R\omega$ (Eq. (8)) achieved experimentally resulted equal to 98.3%

(i.e. $\left(\frac{27.66\ \text{Hz}-13.95\ \text{Hz}}{13.95\ \text{Hz}}\right)\times 100$, indicated by the arrows in Fig. 10). This result is close to the 103% value achieved numerically (Section 4).

Two final remarks should be brought to notice. The first observation to make is that the maximum current value used to achieve the mentioned result for $R\omega$ is much lower than 2 A: this means that an extended frequency range can be achieved employing a low current, in contrast to most of the referenced works where high currents are needed (e.g. [19]). This is made possible by the use of SMA wires, in place of beams. The second observation to make concerns the damping of the whole system (PS+SMA wires): Eq. (24) shows that the SMA wires introduce a force related to the relative displacement between the ATMD mass and the PS mass. Nevertheless, there also is a damping component, related to the damping of the structure composed by the ATMD mass and the SMA wires. This damping force is found to be almost dependent on the relative velocity between the ATMD mass and the PS mass [19] for this set-up. Such a force is low if compared to the damping force provided by the eddy current damper (the ratio between the two forces is higher than 10; see the details for the eddy current damper force in Sections 7 and 8.2). For this reason the authors have decided not to model this additional force which would have made the model more complex without adding significant improvements to its accuracy. Nevertheless, it must be taken into account when the eddy current damper is switched off, in the case numerical results are required to have special accuracy. The damping coefficient related to this additional force can be estimated by different types of tests (e.g. by carrying out a modal analysis of the system composed by the ATMD mass, the SMA wires, and the elastic elements, mounted on a rigid frame) [19] and the change of the force is almost negligible when changing phase from DM to AU (in agreement with [20]). The damping coefficient was estimated equal to 0.2 N/m/s.

8.1.2. Tests of the efficacy of the ATMD to adapt its eigenfrequency

These tests have been carried out following this procedure:

- the ATMD was mistuned at the beginning of the tests;
- the ATMD took a certain amount of time to tune its eigenfrequency;
- the PS was changed by adding – or removing – masses (i.e. m_{PS} is changed) by using magnets. This caused a mistuning between the PS and the ATMD;
- then the ATMD tuned its eigenfrequency again.

The random excitation was provided in the frequency range between 10 and 25 Hz and the corresponding root mean square value of $\ddot{x}_1$ was about 1000 mm/s^2 in mistuned conditions.

Fig. 11 shows the time history of i_w for three changes of m_{PS}. At point L_1 the on-line estimator reaches the steady-state and the controller is activated (from $t=0$ s to $t=L_1$, $i_w=1.05$ A, because for time lower than 0 s the SMA wires are not supplied with current and the actual value of F is assumed to be too low, so that at time 0 s the current is automatically

Table 3
Technical data of the accelerometers used in the experiments.

Sensitivity	Measurement range	Frequency range	Nonlinearity	Transverse sensitivity	Spectral noise (100 Hz)
10.2 mV/m/s^2	$\pm$ 490 m/s^2	2–3000 Hz	$\leq$ 1%	$\leq$ 3%	33 μm/s^2/$\sqrt{\text{Hz}}$

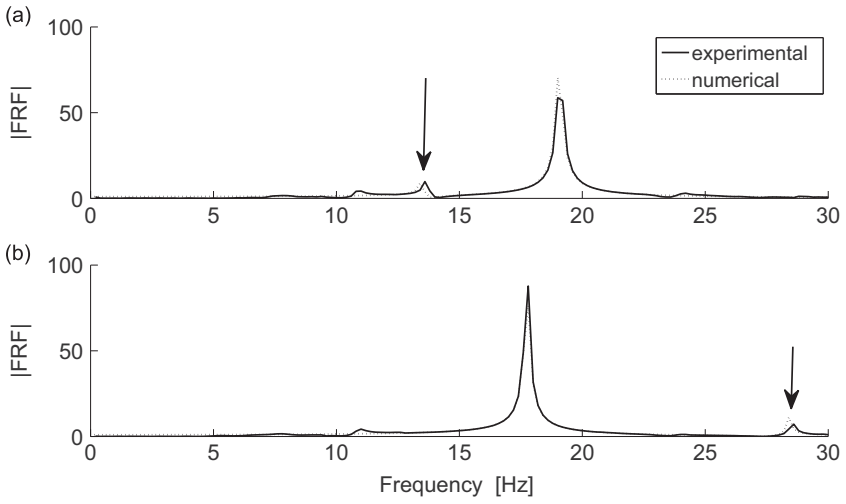

Fig. 10. FRF of the complete system (PS+ATMD) between x_3 and x_1 (i.e. x_1/x_3, see to Fig. 1): 0 A supplied (a) and 1.55 A supplied (b).

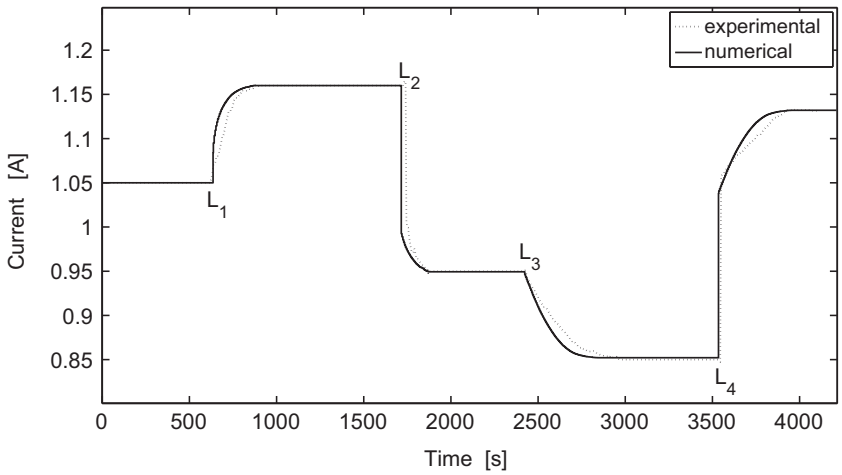

Fig. 11. Time history of i_w.

tuned to 1.05 A. See Section 6.1.2). At point L_2 a mass of 100 g is added to m_{PS}. At point L_3 an additional mass of 100 g is added to m_{PS}. At point L_4 a mass of 200 g is subtracted from m_{PS}.

Fig. 12a and b respectively shows the corresponding FRFs (in steady-state condition) relative to the first tuning and to the first addition of a 100 g mass for APP1. The FRFs for the remaining cases are not shown since the results are similar. The concordance between the experimental and the numerical results is good, further proving the reliability of the model herein developed. Furthermore, the gain-scheduling approach for the control with APP1 proves to be reliable. Hence, the ATMD proves to be capable of following the changes of the PS (Fig. 12a and b).

As for APP2, Fig. 12c and d shows the FRFs in steady-state condition for the same changes of m_{PS} (same as of a and b). Again the numerical results match the experiments and the control strategy proves to effectively follow the changes of the PS. When the variation of the mass m_{PS} is high, employing APP2 makes for a slower adaptation than with APP1. Numerical analyses showed that this result is strongly correlated to the signal-to-noise-ratio of the measured acceleration $\ddot{x}_1$ (i.e. the lower the signal-to-noise-ratio is, the slower the adaptation is). Nevertheless, real systems are seldom affected by changes of their dynamic features as sudden or high as in this case. Therefore, in practical applications, such a drawback could be often neglected.

Table 4 summarises advantages and drawbacks of the two approaches.

Some further facts deserve to be pointed out. The kind of disturbance here taken into consideration is random noise and the displacements at resonance are significantly lower in this case than in the case of a mono-harmonic disturbance, because of the different frequency distribution of the power of the disturbance. This guarantees a much lower probability of having a significant nonlinear behaviour of the ATMD (Eqs. (24) and (25); geometrical nonlinearity) as compared to the case of a mono-harmonic excitation. This latter case would probably lead to a significant geometrical nonlinearity. Therefore, a random disturbance represents a favourable case under this point of view and it seems reasonable to consider the behaviour of the ATMD as nigh linear.

Nevertheless, the model of the ATMD takes into account the nonlinearity as well and it is of general validity. The nonlinear term is neglected when the control of the ATMD is taken into account. Two control strategies are proposed (APP1 and APP2). APP1 is valid as long as the linear approximation is valid and would fail when the nonlinearity tended to become significant. Otherwise, APP2 (which works on the shape of a power-spectrum) is expected to work properly also in presence of moderate nonlinearity. Indeed, as for the frequency representation of nonlinear structures, random excitation applies a linearisation procedure to the behaviour of the structure, which is considered to provide an optimised linear model for the test structure [43]. This means that the empirical approach of APP2 should not suffer too much from a moderate nonlinear behaviour and would be still able to provide an attenuation of the average vibration of the PS. Of course, when the nonlinear behaviour becomes dominant the frequency representation fails and a different control approach must be used, but this is considered out of the scope of this paper. Different works on nonlinear TMDs are already available in literature (e.g. [36]) and they can be employed to properly drive the features of this ATMD. It may be mentioned that the problem of nonlinearity in presence of high displacements does rise in most of the works on TMDs based on SMA referenced in this paper.

8.2. Tests with the damper

These tests have been carried out by adjusting the damping provided by the eddy current damper as soon as the SMA wires are tuned (i.e. the eigenfrequency is tuned). For sake of conciseness, only results from a test with APP2 are here reported, since similar outcomes resulted by using APP1.

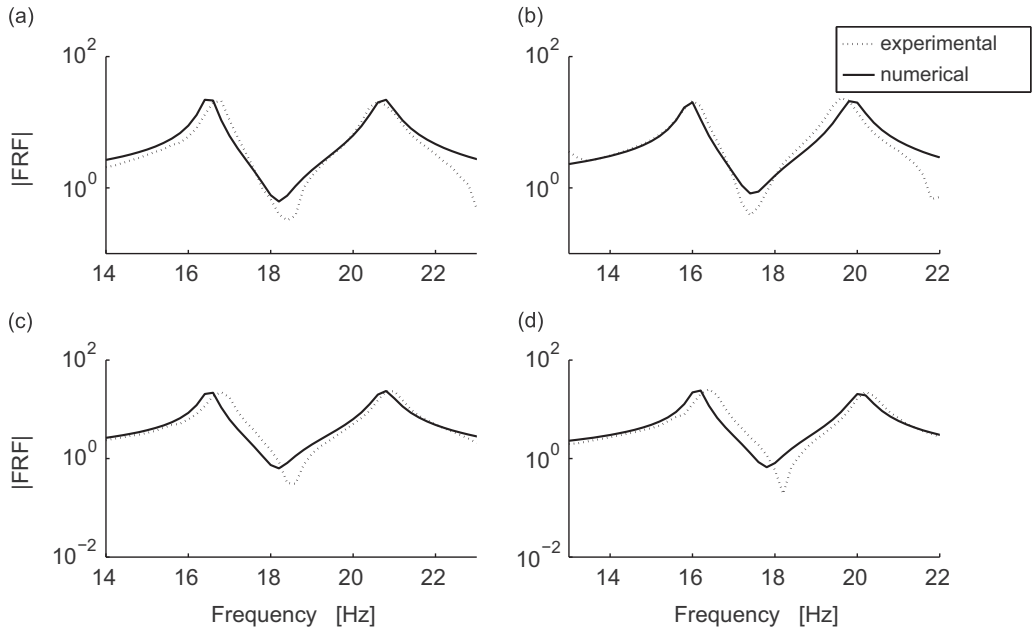

Fig. 12. FRF between x_3 and x_1 (i.e. x_1/x_3, see to Fig. 1): first tuning with APP1 (a), tuning after the addition of the first 100 g with APP1 (b), first tuning with APP2 (c), tuning after the addition of the first 100 g with APP2 (d).

Table 4
Advantages and drawbacks of APP1 and APP2.

APP1	APP2
Advantages: no model of the system is needed, quick tuning of the system, robust to disturbances *Drawbacks*: 3 signals to measure (one of them is either the vibration of the constraint or the force acting on the PS), implementation more complex than APP2	*Advantages*: 1 signal to measure, no model of the system is needed, easy to implement *Drawbacks*: Adaptation time dependent on the signal-to-noise ratio of the measured signal, the random disturbance must be close to white random noise

Fig. 13a shows the FRF between x_3 and x_1 (for the case of PS added with a mass of 100 g) after the eddy current damper reached the steady-state condition. Although the numerical and experimental FRFs provided in Fig. 13a match closely, the current required by the eddy current damper is quite different (0.74 A in the experimental case and 0.45 A in the simulations): this is due to inaccuracies in the model of the damper, mainly due to inaccuracies in foreseeing the behaviour of the permanent magnet and the value of the magnetic field at the air-gap, which is affected by unpredicted dispersion of the flux. Nevertheless, the feed-back algorithm proposed in Section 6.1.3 proved to work properly, achieving a good dynamic behaviour in the frequency range around the PS resonance.

Finally, Fig. 13b shows some experimental FRFs between x_3 and x_1 in order to gain clear understanding of the effect of the ATMD. Two of them show the behaviour of the original PS (with the addition of a mass of 200 g): without the ATMD (dash-dot line in the figure), and with the ATMD mounted and switched off (dotted line). The other two FRFs show the behaviour of the PS with the maximum added mass during the tests (i.e. 200 g) with the ATMD mounted and in two different configurations: with the SMA wires switched on and in steady state after adaptation and the eddy current damper switched off (dashed line), and then with both the devices switched on and in steady state after adaptation (solid line).

It should be noted that the ATMD cannot adapt its dynamic features in case of power failure. This means that the ATMD dynamic features must be tuned on those of the PS at environmental temperature (i.e. with no power supply to the SMA wires) if a vibration attenuation is desired even in case of power failure. In this scenario, the eigenfrequency of the ATMD can follow the changes of the PS eigenfrequency only if this latter parameter increases.

9. Conclusion

This paper has illustrated a new type of adaptive tuned mass damper based on shape memory alloys and eddy current damping. The former element is used to adapt the eigenfrequency of the device, while the latter to tune the damping.

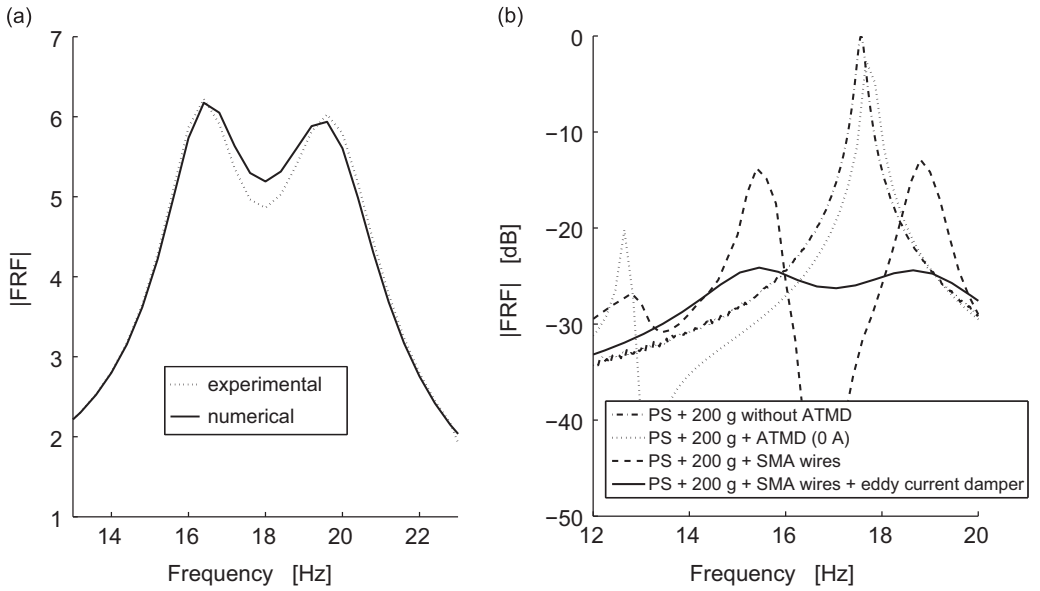

Fig. 13. FRF between x_3 and x_1 (i.e. x_1/x_3, see to Fig. 1) with the activation of the damping control. The starting condition for figure (a) is that of Fig. 12c (i.e. with a mass of 100 g added), where the tuning of ω_{ATMD} is already achieved. Instead, figure (b) shows different FRFs with and without ATMD, for a direct comparison.

The device proves to have a wide adaptation range in terms of eigenfrequency (about 100%), achieved by changing the axial load of the shape memory alloy wires. The approach does not rely on changing Young's modulus, which would require high performance materials. Hence, in the design herein proposed any kind of shape memory alloy can be used to achieve a wide frequency range. Furthermore, low values of current are needed to reach this goal.

Two different adaptation strategies have been developed and compared: one relying on closed optimal formulas, and the other on an empiric approach. The advantages and drawbacks have been highlighted in both cases. Furthermore, the model developed to simulate the dynamic behaviour of the SMA wires has proven to be reliable so that it can be used for model-based controllers.

Acknowledgements

The authors would like to thank Dr. Paola Bassani of CNR-IENI (Lecco, Italy) for the support in carrying out the characterisation of the SMA wires and SAES Getters for having provided the SMA wires.

Appendix A

This appendix defines the symbols b and y in Eq. (34):

$$b = -\frac{\alpha}{\frac{A_{w1}}{KL_w}+\frac{1}{E_{w,\mathrm{AU}}-\xi\left(E_{w,\mathrm{AU}}-E_{w,\mathrm{DM}}\right)}} \tag{A1}$$

$$y = \frac{\sigma_{w,0}\left(\frac{A_{w1}}{KL_w}+\frac{1}{E_{w,\mathrm{DM}}}\right)+\alpha T_0+H^{\mathrm{cur}}(1-\xi)}{\frac{A_{w1}}{KL_w}+\frac{1}{E_{w,\mathrm{AU}}-\xi\left(E_{w,\mathrm{AU}}-E_{w,\mathrm{DM}}\right)}} \tag{A2}$$

Appendix B

This appendix defines the symbols in Eq. (35):

$$a_d = G_d B_d; \quad b_{1,d} = G_d A_d + 1 + H_d B_d; \quad b_{2,d} = G_d C_d + B_d I_d; \quad c_{1,d} = H_d A_d; \quad c_{2,d} = H_d C_d + I_d A_d; \quad c_{3,d} = C_d I_d \tag{B1}$$

where

$$K^* = -\left(\frac{A_{w1}}{KL_w}+\frac{1}{E_{w,\mathrm{DM}}}\right); \quad A_d = E_{w,\mathrm{AU}} + \Delta E \xi_{-1} + \frac{M_S \Delta E}{M_S - M_f}(1-\xi_{-1});$$

$$B_d = \frac{\Delta E}{C_M(M_S - M_f)}(1-\xi_{-1}); \quad C_d = -\frac{\Delta E}{(M_S - M_f)}(1-\xi_{-1});$$
$$D_d = -H^{\mathrm{cur}} + \xi_{-1}H^{\mathrm{cur}} + \frac{M_S H^{\mathrm{cur}}}{M_S - M_f}(1-\xi_{-1}); \quad E_d = \frac{H^{\mathrm{cur}}}{C_M(M_S - M_f)}(1-\xi_{-1});$$
$$F_d = -\frac{H^{\mathrm{cur}}}{(M_S - M_f)}(1-\xi_{-1}); \quad G_d = \frac{A_{w1}}{KL_w} + E_d;$$
$$H_d = K^*\sigma_{w,0} - \alpha T_0 + D_d; \quad I_d = \alpha + F_d; \quad \Delta E = E_{w,\mathrm{AU}} - E_{w,\mathrm{DM}} \tag{B2}$$

And the symbols in Eq. (36)

$$a_i = G_i B_i; \quad b_{1,i} = G_i A_i + 1 + H_i B_i; \quad b_{2,i} = G_i C_i + B_i I_i;$$
$$c_{1,i} = H_i A_i; \quad c_{2,i} = H_i C_i + I_i A_i; \quad c_{3,i} = C_i I_i; \tag{B3}$$

where

$$K^* = -\left(\frac{A_{w1}}{KL_w} + \frac{1}{E_{w,\mathrm{DM}}}\right); \quad A_i = E_{w,\mathrm{DM}} + \Delta E\xi_{-1} + \frac{A_f \Delta E}{A_f - A_s}(1-\xi_{-1});$$
$$B_i = \frac{\Delta E}{C_A(A_f - A_s)}(1-\xi_{-1}); \quad C_i = -\frac{\Delta E}{(A_f - A_s)}(1-\xi_{-1});$$
$$D_i = -H^{\mathrm{cur}} + \xi_{-1}H^{\mathrm{cur}} + \frac{A_f H^{\mathrm{cur}}}{A_f - A_s}(1-\xi_{-1}); \quad E_i = \frac{H^{\mathrm{cur}}}{C_A(A_f - A_s)}(1-\xi_{-1});$$
$$F_i = -\frac{H^{\mathrm{cur}}}{(A_f - A_s)}(1-\xi_{-1}); \quad G_i = \frac{A_{w1}}{KL_w} + E_i;$$
$$H_i = K^*\sigma_{w,0} - \alpha T_0 + D_i; \quad I_i = \alpha + F_i; \quad \Delta E = E_{w,\mathrm{AU}} - E_{w,\mathrm{DM}} \tag{B4}$$

Appendix C

This appendix defines the symbols in Eq. (41)

$$A_{s,d} = {b_{1,d}}^2 - 4a_d c_{1,d}; \quad B_{s,d} = 2b_{1,d}b_{2,d} - 4a_d c_{2,d}; \quad C_{s,d} = {b_{2,d}}^2 - 4a_d c_{3,d} \tag{C1}$$

and Eq. (42)

$$A_{s,i} = b_{1,i}^2 - 4a_i c_{1,i}; \quad B_{s,i} = 2b_{1,i}b_{2,i} - 4a_i c_{2,i}; \quad C_{s,i} = {b_{2,i}}^2 - 4a_i c_{3,i}; \tag{C2}$$

References

[1] H. Frahm, Device for damping vibrations of bodies, 989958, 1909.
[2] S. Krenk, J. Høgsberg, Tuned mass absorbers on damped structures under random load, *Probabilistic Engineering Mechanics* 23 (2008) 408–415, http://dx.doi.org/10.1016/j.probengmech.2007.04.004.
[3] A. Mohtat, E. Dehghan-Niri, Generalized framework for robust design of tuned mass damper systems, *Journal of Sound and Vibration* 330 (2011) 902–922, http://dx.doi.org/10.1016/j.jsv.2010.09.007.
[4] C.J. Longbottom, M.J. Day, E. Rider, A self tuning vibration absorber, GB218957B, 1990.
[5] T. Long, M.J. Brennan, S.J. Elliott, Design of smart machinery installations to reduce transmitted vibrations by adaptive modification of internal forces, *Proceedings of the Institution of Mechanical Engineers, Part I: Journal of Systems and Control Engineering* 212 (1998) 215–228, http://dx.doi.org/10.1243/0959651981539415.
[6] P. Bonello, M.J. Brennan, S.J. Elliott, Vibration control using an adaptive tuned vibration absorber with a variable curvature stiffness element, *Smart Materials and Structures* 14 (2005) 1055–1065, http://dx.doi.org/10.1088/0964-1726/14/5/044.
[7] D. Gsell, G. Feltrin, M. Motavalli, Adaptive tuned mass damper based on pre-stressable leaf-springs, *Journal of Intelligent Material Systems and Structures* 18 (2007) 845–851, http://dx.doi.org/10.1177/1045389X06073641.
[8] J.P. Carneal, F. Charette, C.R. Fuller, Minimization of sound radiation from plates using adaptive tuned vibration absorbers, *Journal of Sound and Vibration* 270 (2004) 781–792, http://dx.doi.org/10.1016/S0022-460X(03)00257-8.
[9] M.J. Brennan, Actuators for active control – tunableresonant devices, *Applied Mechanics and Engineering* 5 (2000) 63–74.
[10] N. Carpineto, W. Lacarbonara, F. Vestroni, Hysteretic tuned mass dampers for structural vibration mitigation, *Journal of Sound and Vibration* 333 (2014) 1302–1318, http://dx.doi.org/10.1016/j.jsv.2013.10.010.
[11] F. Weber, C. Boston, M. Maślanka, An adaptive tuned mass damper based on the emulation of positive and negative stiffness with an MR damper, *Smart Materials and Structures* 20 (2011) 015012, http://dx.doi.org/10.1088/0964-1726/20/1/015012.
[12] F. Weber, M. Maślanka, Frequency and damping adaptation of a TMD with controlled MR damper, *Smart Materials and Structures* 21 (2012) 055011, http://dx.doi.org/10.1088/0964-1726/21/5/055011.
[13] O. Heuss, R. Salloum, D. Mayer, T. Melz, Tuning of a vibration absorber with shunted piezoelectric transducers, *Archive of Applied Mechanics* (2014) 1–18, http://dx.doi.org/10.1007/s00419-014-0972-5, in press.
[14] M.A. Savi, a.S. De Paula, D.C. Lagoudas, Numerical investigation of an adaptive vibration absorber using shape memory alloys, *Journal of Intelligent Material Systems and Structures* 22 (2010) 67–80, http://dx.doi.org/10.1177/1045389X10392612.
[15] R.a. Aguiar, M.a. Savi, P.M. Pacheco, Experimental investigation of vibration reduction using shape memory alloys, *Journal of Intelligent Material Systems and Structures* 24 (2012) 247–261, http://dx.doi.org/10.1177/1045389X12461696.

[16] B. Tiseo, A. Concilio, S. Ameduri, A. Gianvito, A shape memory allous based tunable dynamic vibration absorber for vibration tonal control, *Journal of Theoretical and Applied Mechanics* 48 (2010) 135–153.
[17] Y. Mani, M. Senthilkumar, Shape memory alloy based adaptive-passive dynamic vibration absorber for vibration control in piping applications, *Journal of Vibration and Control* (2013), http://dx.doi.org/10.1177/1077546313492183, in press.
[18] X. Zuo, A. Li, Numerical and experimental investigation on cable vibration mitigation using shape memory alloy damper, *Structural Control and Health Monitoring* 18 (1) (2011) 20–39, http://dx.doi.org/10.1002/stc.
[19] E. Rustighi, M.J. Brennan, B.R. Mace, Real-time control of a shape memory alloy adaptive tuned vibration absorber, *Smart Materials and Structures* 14 (2005) 1184–1195, http://dx.doi.org/10.1088/0964-1726/14/6/011.
[20] E. Rustighi, M.J. Brennan, B.R. Mace, A shape memory alloy adaptive tuned vibration absorber: design and implementation, *Smart Materials and Structures* 14 (2005) 19–28, http://dx.doi.org/10.1088/0964-1726/14/1/002.
[21] O.E. Ozbulut, C. Mir, M.O. Moroni, M. Sarrazin, P.N. Roschke, A fuzzy model of superelastic shape memory alloys for vibration control in civil engineering applications, *Smart Materials and Structures* 16 (2007) 818–829, http://dx.doi.org/10.1088/0964-1726/16/3/031.
[22] C. Mavroidis, Development of advanced actuators using shape memory alloys and electrorheological fluids, *Research in Nondestructive Evaluation* 14 (2002) 1–32, http://dx.doi.org/10.1007/s00164-001-0018-6.
[23] P. Senthilkumar, M. Umapathy, Use of load generated by a shape memory alloy for its position control with a neural network estimator, *Journal of Vibration and Control* 20 (11) (2014) 1707–1717, http://dx.doi.org/10.1177/1077546313481000.
[24] K. Williams, G. Chiu, R. Bernhard, Adaptive-passive absorbers using shape-memory alloys, *Journal of Sound and Vibration* 249 (2002) 835–848, http://dx.doi.org/10.1006/jsvi.2000.3496.
[25] K.A. Williams, G.T.C. Chiu, R.J. Bernhard, Nonlinear control of a shape memory alloy adaptive tuned vibration absorber, *Journal of Sound and Vibration* 288 (2005) 1131–1155, http://dx.doi.org/10.1016/j.jsv.2005.01.018.
[26] H. Dai, Z. Huang, W. Wang, A new permanent magnetic friction damper device for passive energy dissipation, *Smart Materials and Structures* 23 (2014) 105016, http://dx.doi.org/10.1088/0964-1726/23/10/105016.
[27] J.-L. Chen, C.T. Georgakis, Spherical tuned liquid damper for vibration control in wind turbines, *Journal of Vibration and Control* (2013), http://dx.doi.org/10.1177/1077546313495911, in press.
[28] Z. Zhang, B. Basu, S.R.K. Nielsen, Tuned liquid column dampers for mitigation of edgewise vibrations in rotating wind turbine blades, *Structural Control and Health Monitoring* 20 (3) (2015) 500–517, http://dx.doi.org/10.1002/stc.1689.
[29] J. Chen, C.T. Georgakis, Tuned rolling-ball dampers for vibration control in wind turbines, *Journal of Sound and Vibration* 332 (2013) 5271–5282, http://dx.doi.org/10.1016/j.jsv.2013.05.019.
[30] D.C. Lagoudas, *Shape Memory Alloys: Modeling and Engineering Applications*, Springer, New York, 2008.
[31] H.A. Sodano, D.J. Inman, Non-contact vibration control system employing an active eddy current damper, *Journal of Sound and Vibration* 305 (2007) 596–613, http://dx.doi.org/10.1016/j.jsv.2007.04.050.
[32] J.S. Bae, M.K. Kwak, D.J. Inman, Vibration suppression of a cantilever beam using eddy current damper, *Journal of Sound and Vibration* 284 (2005) 805–824, http://dx.doi.org/10.1016/j.jsv.2004.07.031.
[33] S. Mirzaei, Flexible electromagnetic damper, *Proceedings of IEEE International Electric Machines and Drive Conference 2007. IEMDC '07*, Vol. 2, Antalya, 2007, pp. 959–962.
[34] L. Meirovitch, *Fundamentals of Vibrations*, McGraw-Hill, New York, 2001.
[35] M.a. Acar, C. Yilmaz, Design of an adaptive–passive dynamic vibration absorber composed of a string–mass system equipped with negative stiffness tension adjusting mechanism, *Journal of Sound and Vibration* 332 (2013) 231–245, http://dx.doi.org/10.1016/j.jsv.2012.09.007.
[36] N.a. Alexander, F. Schilder, Exploring the performance of a nonlinear tuned mass damper, *Journal of Sound and Vibration* 319 (2009) 445–462, http://dx.doi.org/10.1016/j.jsv.2008.05.018.
[37] Y.A. Cengel, *Introduction to Thermodynamics and Heat Transfer*, 2nd ed. McGraw-Hill, 2009.
[38] J. Ormondroyd, J.P. Den Hartog, The theory of the dynamic vibration absorber, *Transaction of the American Society of Mechanical Engineers* 50 (1928) 9–22.
[39] J.J.E. Slotine, W. Li, *Applied Nonlinear Control*, Prentice-Hall, Englewood Cliffs, 1991.
[40] R.S. Burns, *Advanced Control Engineering*, Butterworth-Heinemann, Oxford, 2001.
[41] J.S. Bendat, A.G. Piersol, *Random Data: Analysis and Measurement Procedures*, fourth edition, Wiley, Hoboken, 2010.
[42] E. Doebelin, *Measurement Systems: Application and Design*, McGraw-Hill, 2003.
[43] D.J. Ewins, *modal Testing: Theory, Practice and Application*, second edition, Research Studies Press Ltd., Baldock, 2000.